



# The Intracuster Light of Abell 3667: Unveiling an Optical Bridge in LSST Precursor Data

Anthony M. Englert<sup>1</sup> , Ian Dell’Antonio<sup>1</sup> , and Mireia Montes<sup>2</sup>

<sup>1</sup> Department of Physics, Brown University, Providence, RI 02912, USA

<sup>2</sup> Institute of Space Sciences (ICE, CSIC), Campus UAB, Carrer de Can Magrans, s/n, 08193 Barcelona, Spain

Received 2025 April 22; revised 2025 May 28; accepted 2025 May 30; published 2025 August 5

## Abstract

Intracuster light (ICL), the diffuse glow of stars stripped from galaxies during a cluster’s formation, is an established tracer of a cluster’s dynamical history. The upcoming Vera C. Rubin Observatory’s Legacy Survey of Space and Time (LSST) is set to revolutionize studies of ICL by imaging the entire southern sky down to a limiting surface brightness  $\mu \gtrsim 30$  mag arcsec<sup>−2</sup> by year 10. In this Letter, we create a precursor LSST data set (reaching the equivalent of year 8 depth) using Dark Energy Camera observations of Abell 3667 (A3667) and study its ICL. We have discovered a low surface brightness ( $\mu \gtrsim 26$  mag arcsec<sup>−2</sup>) optical bridge extending over  $\sim 400$  kpc, which connects the two brightest galaxies (BCG1 and BCG2) in the cluster; the color and surface brightness of the bridge is consistent with formation via a major merger. The inner regions of BCG1 ( $r < 200$  kpc) and BCG2 ( $r < 50$  kpc) are consistent with formation via gradual stripping of satellite galaxies, but BCG2’s outer profile appears disrupted by a recent merger. We hypothesize that the bridge is a relic of a recent first pass between the two brightest galaxies and is composed of stars being stripped from BCG2. Future studies of ICL with LSST will discover new features such as the bridge in local clusters while enabling detailed studies of the stellar populations of these features with its six photometric bands.

*Unified Astronomy Thesaurus concepts:* Galaxy clusters (584); Abell clusters (9); Galaxy mergers (608); Ground-based astronomy (686)

## 1. Introduction

Galaxy clusters are among the largest gravitationally bound objects in the Universe and span a variety of dynamical states, ranging from recent mergers to fully virialized systems (A. V. Kravtsov & S. Borgani 2012). Actively merging clusters in particular can be used to constrain the nature of dark matter (D. Clowe et al. 2006; D. Harvey et al. 2015) and probe cosmology (S. W. Allen et al. 2011). They show abundant evidence of their history through diffuse X-ray and radio emissions arising from interactions within the intracluster medium (C. L. Sarazin 1986; R. J. van Weeren et al. 2019). These emissions can be used to infer the dynamical history based on the presence of radio relics (W. Lee et al. 2024; K. Finner et al. 2025) or X-ray features such as shock fronts (C. L. Sarazin 1986). In optical studies, a complementary tracer of a cluster’s dynamical history is the intracluster light (ICL).

ICL is the combined emission of individual stars that have been stripped from cluster members by tidal forces throughout the cluster’s formation (E. Contini 2021; M. Montes 2022). It is a feature in the low surface brightness (LSB) regime, with characteristic surface brightnesses fainter than  $\mu_V \sim 26$  mag arcsec<sup>−2</sup>, and is often observed by studying the surface brightness profile of a brightest cluster galaxy (BCG) out to large distances ( $\gtrsim 100$  kpc) from the core. The ICL is an established tracer for the distribution of dark matter across a cluster (M. Montes & I. Trujillo 2019; I. Alonso Asensio et al. 2020; H. Sampaio-Santos et al. 2021; J. Yoo et al. 2022;

J. M. Diego et al. 2023; J. Yoo et al. 2024; S. Cha et al. 2025), and by studying the surface brightness profile and color profiles of the combined BCG+ICL system, the dynamical history of a cluster can be inferred.

The ICL can form through various “formation channels;” the most relevant ones for this Letter are the stellar stripping and merger scenarios. In the stellar stripping scenario, ICL is formed from the stripping of stars from satellite galaxies near the BCG. This occurs gradually as the cluster evolves, so older and lower-metallicity stars stripped early in the cluster’s history will be closer to the core of the BCG, creating a negative color gradient (from red to blue) across the profile of the BCG+ICL system (M. Montes & I. Trujillo 2014; T. DeMaio et al. 2015, 2018; E. Contini et al. 2018; M. Montes et al. 2021). In the merger scenario, ICL is formed from the rapid stripping of stars from galaxies during a merger; this mixes the ages and metallicities of stars across the ICL, producing a flat color profile (M. Montes & I. Trujillo 2018; E. Contini 2021). The distinct impact of these formation channels can be used to infer the presence of mergers in a cluster’s dynamical history (J. C. Mihos et al. 2016; E. Iodice et al. 2017; T. DeMaio et al. 2018; M. Montes & I. Trujillo 2022).

Abell 3667 (A3667) is an actively merging cluster featuring complex X-ray emissions and prominent radio relics (L. Lovisari et al. 2009; M. S. Owers et al. 2009; E. Carretti et al. 2013; E. Storm et al. 2018; F. de Gasperin et al. 2022). Currently, the leading hypothesis is that A3667 is the product of an offset intermediate-mass merger, which can simultaneously explain the origin of the radio relics and the structure of the X-ray emissions (F. de Gasperin et al. 2022; Y. Omiya et al. 2024). Studying the ICL of A3667 offers a compelling alternate method of confirming this hypothesis. However, A3667’s low redshift ( $z = 0.0556$ )



Original content from this work may be used under the terms of the [Creative Commons Attribution 4.0 licence](https://creativecommons.org/licenses/by/4.0/). Any further distribution of this work must maintain attribution to the author(s) and the title of the work, journal citation and DOI.

constrains this analysis to deep-wide ground-based imaging where the large field of view can capture the ICL.

Generally, ICL studies originate from either space-bound observations of high-redshift ( $z > 0.1$ ) clusters (M. Montes & I. Trujillo 2014, 2022, 2018; C. Burke et al. 2015; T. Morishita et al. 2017; Y. Jiménez-Teja et al. 2018; A. H. Gonzalez et al. 2021; N. S. Martis et al. 2024; A. Ellien et al. 2025) or from ground-based observations of local clusters with deep-wide field imaging (A. H. Gonzalez et al. 2005; J. C. Mihos et al. 2005; E. Iodice et al. 2017; Y. Zhang et al. 2019; M. Kluge et al. 2020; M. Montes et al. 2021; Y. Jiménez-Teja et al. 2025). The Rubin Observatory’s Legacy Survey of Space and Time (LSST) is set to revolutionize ICL studies of local clusters by observing the entire southern sky down to a limiting surface brightness of at least  $\mu \simeq 30.3$  mag arcsec<sup>-2</sup> by year 10 (F. B. Bianco et al. 2022; S. Brough et al. 2024). Since the LSST Science Pipelines (LSP) are built to process data from multiple observatories (J. Bosch et al. 2018, 2019), precursor data sets of similar depth can be built using the latest algorithms intended for LSST (H. Aihara et al. 2018; S. Fu et al. 2022; Y. Luo et al. 2024).

In this Letter, we present a precursor LSST data set for A3667 and study its ICL; the remainder of the Letter is structured as follows. In Section 2, we summarize our observations, implementation of the LSP, and post-LSP processing steps to create coadds suitable for LSB science. In Section 3, we characterize the ICL of A3667, and in Section 4, we discuss how this is related to the cluster’s dynamical history. Throughout, we use the AB magnitude system (J. B. Oke & J. E. Gunn 1983) and assume a concordance  $\Lambda$ CDM cosmology with  $H_0 = 70$  km s<sup>-1</sup> Mpc,  $\Omega_m = 0.3$ , and  $\Omega_\Lambda = 0.7$ . This produces a distance-scale of 1.08 kpc arcsec<sup>-1</sup> at  $z = 0.0556$ .

## 2. Data and Processing

### 2.1. Observations and Data Processing

We used observations taken by the Dark Energy Camera (DECam) on the 4 m Blanco Telescope at the Cerro Tololo Inter-American Observatory (B. Flaugher et al. 2015). We queried all public raw exposures taken in the *ugriz* bands from the NOIRLab Astro Data Archive within 2° of the X-ray luminosity peak based on the Meta Catalog of X-Ray Clusters (R. Piffaretti et al. 2011). This query was wide enough to include stray pointings whose detectors overlap with the virial radius of the cluster ( $\lesssim 1$  Mpc of the X-ray peak), maximizing our depth in this region. A table of the proposal IDs, PIs, and exposure times are provided in Appendix C.

Raw exposures were processed using a modified version of the `run_steps` script built by the Local Volume Complete Cluster Survey (S. Fu et al. 2022), which has been adapted to v26\_0\_0 of the LSP (A. Englert et al. 2024, 2025). Our implementation of the Data Release Pipeline for DECam<sup>3</sup> includes two additional features: a correction for the brighter-fatter effect (W. R. Coulton et al. 2018; A. Broughton et al. 2024) and an implementation of the `skycorr` algorithm originally built for the Hyper Suprime-Cam (HSC) on the Subaru Telescope (H. Aihara et al. 2019, 2022). Monthly bias and flat frames were built with the LSP’s calibration-products pipeline<sup>4</sup> and

span the past decade of DECam’s observations starting from the Dark Energy Survey (The Dark Energy Survey Collaboration et al. 2016). These have been uploaded to Rubin Observatory’s US Data Facility and are available upon request. A discussion of our photometric calibration has been summarized in Appendix A.

Background modeling has remained a challenge for ground-based deep-wide observations due to difficulties in separating extended LSB features (such as Galactic cirri or ICL) from the true background in calibrated exposures (J. Román et al. 2020; J. Li et al. 2022). To address this, `skycorr` removes the background by masking detected sources, subtracting a large-scale gradient and a fitted skyframe, and subtracting a small-scale local background (`bgmodel2`). The detection and background subtraction steps are iterated until the background converges; then, the resulting “sky-corrected” exposures are stacked to produce a coadd (Figure 1). Like previous studies, we found that `bgmodel2` caused oversubtraction around the largest LSB features (J. Li et al. 2022) and disabled it during processing. This led to artifacts in the *i* band and, to a lesser extent, the *z* band, due to their more complex sky backgrounds. Therefore, we limited our analysis of the ICL to the *g* and *r* bands while relying on *grz* images for detection and manual inspection for features. A detailed discussion of our implementation of `skycorr` is provided in Appendix B.

### 2.2. LSB Considerations

LSB science benefits greatly from dedicated observing strategies designed to minimize the background, including strategies such as creating sky flats (A. Borlaff et al. 2019) or specialized dither patterns (I. Trujillo & J. Fliri 2016). Since our study uses archival data, we cannot apply these specialized observing strategies; we did, however, carry out extensive quality checks on each frame. Each exposure was manually inspected for defects, and tight constraints were placed on the data that were stacked, including cuts on the seeing (see S. Fu et al. 2022). Additionally, we stacked exposures taken almost exclusively during dark time; for the <7% of frames taken during gray time, the moon was >30° from the target. Although no dedicated observing strategy was applied, previous proposals used dither patterns sufficient to cover DECam’s  $\sim 1'$  chip gaps.

The use of dome flats can contribute to large- and small-scale variations in the background due to an uneven illumination (e.g., J. J. Feldmeier et al. 2002; A. Borlaff et al. 2019; M. Montes et al. 2021); both of these sources of uncertainty are implicitly included in our limiting surface brightness (Section 3). The monthly flats were manually inspected to verify that they were free of defects. We also executed a test to verify their stability: each pixel was normalized according to the mean flux across its detector; then, the ratio of normalized flats from adjacent months was computed. Assuming that the flats are stable, their ratios should have a mean ( $\bar{r}$ ) near unity with a small standard deviation ( $\sigma_r$ ). We found that, per detector, successive flats were consistent to within  $|1 - \bar{r}| \lesssim 10^{-5}$  with standard deviations  $\sigma_r \lesssim 10^{-3}$ . The quality of individual flats were verified similarly: per detector, the normalized flats have standard deviations  $\lesssim 10^{-2}$ , i.e., they are uniform down to  $\lesssim 1\%$  of the mean flux across a detector.

<sup>3</sup> <https://github.com/lst/drpipe>

<sup>4</sup> <https://github.com/lst/cpipe>



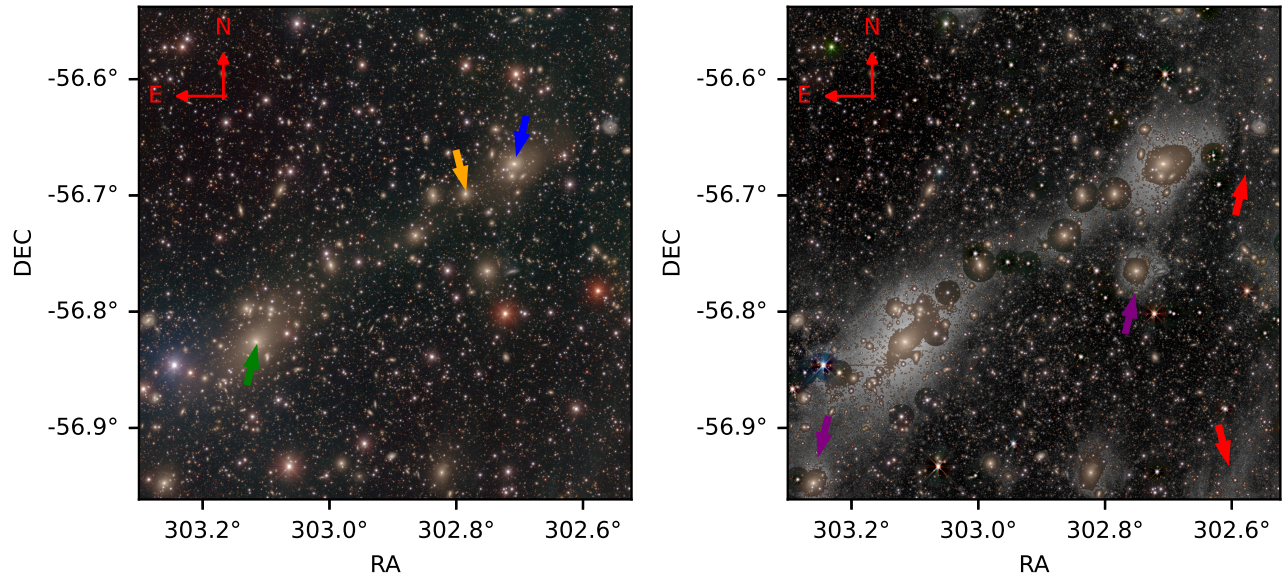


**Figure 1.** Left: a *grz* cutout of our sky-corrected coadd centered on the midpoint between BCG1 (green) and BCG2 (blue). An intermediate galaxy whose profile we study, LEDA 64218, is also labeled (yellow). Right: a cutout of the same field from the sky-corrected and star-subtracted coadd with masked pixels (detections and stars) rendered in *grz*. The pixels rendered in grayscale show the *r*-band coadd with an aggressive stretch to showcase LSB features. Note the presence of cirrus clouds (red) and two cluster members that are enveloped by ICL (purple), LEDA 64290 in the southeast, and LEDA 95791 in the west.

### 2.3. Star Subtraction

Our implementation of `skycorr` preserves even undesirable LSB features, including the wings of the extended point-spread function (PSF), which overlap significantly with the ICL and will bias any measurements if left unaddressed. To remove the wings, we built a model of the extended PSF based on the brightest star in our coadd. After masking background sources and regions near the star with prominent LSB features, we fit a Moffat profile (A. F. J. Moffat 1969) to the core ( $r < 200$  px) and an exponential profile to the wings independently. These were spliced together according to the procedure outlined in R. Infante-Sainz et al. (2020).

To find the scaling of the PSF for a given star ( $a$ ), we computed each star’s radial profile ( $f_*(r)$ ) and fitted it to the extended PSF ( $f(r)$ ) by minimizing the  $\chi^2$ :

$$\chi^2 = \sum_i (f_*(r_i) - af(r_i))^2. \quad (1)$$

By fitting to a radial profile, rather than running a per-pixel optimization, our fit is less likely to be contaminated by background sources obscured by the extended PSF (M. Montes et al. 2021). Moreover, using SExtractor’s segmentation image (E. Bertin & S. Arnouts 1996), we masked background sources, fitted and subtracted the model PSF, and iterated this until convergence. We found that two iterations were sufficient to converge on a reasonable profile for each star.

The PSF was modeled for each band individually; fitting and subtraction was carried out for all stars brighter than the 14th magnitude in *g* centered on their Gaia coordinates (Gaia Collaboration et al. 2023). This model does not account for variations in the PSF across the focal plane of each exposure. Therefore, we limited our subtraction and overall analysis to the central  $0.88 \times 0.88$  (12,000 px  $\times$  12,000 px) region of the coadd, where the PSF is approximately symmetrical and shows little variation.

### 2.4. Masking

LSB science requires aggressive masking to avoid contamination from background and foreground sources that can obscure the extended features of interest. To mask these contaminants, we exported the detection and bad-pixel masks from the LSP. Additionally, to cover the diffraction spikes and other residuals not modeled by our radial PSF model, we masked all pixels within  $\sim 39''$  (150 px) of the core of each bright star.

Studying the profiles of BCGs and other galaxies in the field requires more care since contaminants will blend with and bias the measured profile. We used SExtractor’s segmentation image to mask objects other than the target galaxy, fitted and subtracted a Sérsic to the target, and iteratively masked/subtracted until the mask converged; we found that two iterations were sufficient. Each mask was inspected, and any sources this algorithm missed were manually masked.

## 3. ICL of A3667

### 3.1. LSB Features

Cutouts of our coadds are presented in Figure 1. The BCGs are connected by an optical bridge and feature several prominent plumes connecting them to other cluster members. Galactic cirrus is also present and can be distinguished from the ICL by its morphology, color, and distance from the BCGs.

To study the observed surface brightness of these features, we created LSB contours in the *g* and *r* bands. These were created from the masked and star-subtracted coadds, which were binned into  $16 \text{ px} \times 16 \text{ px}$  superpixels and smoothed with a  $\sigma = 3$  superpixel Gaussian filter. The limiting surface brightness was computed from the sky-corrected, but not star-subtracted, coadd following the procedure outlined in J. Román et al. (2020) and is quoted for  $3\sigma$  detections in  $10'' \times 10''$  squares (Figure 2). Since they are not representative of background pixels, the detected sources, ICL, and galactic cirri were masked during this calculation.

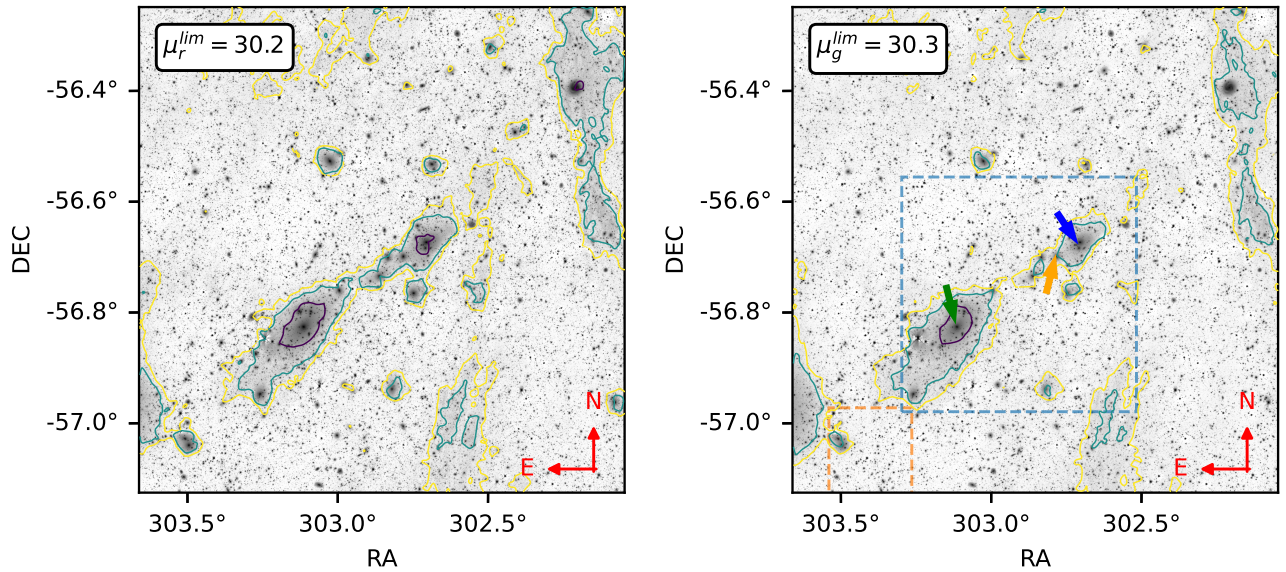


**Figure 2.** LSB contours of the central region of our coadds in  $g$  band (right) and  $r$  band (left) drawn at surface brightnesses of 26, 28, and 30 mag arcsec $^{-2}$ . These are drawn over the corresponding inverted star-subtracted coadd for each band. The eastern LSB feature is the extended PSF of a bright star outside the central region; the northernmost, northwestern, and southernmost 30 mag arcsec $^{-2}$  contours are cirrus (the last two are also highlighted in Figure 1). BCG1 (green), BCG2 (blue), and LEDA 64218 (orange) are labeled in the right panel. Additionally, the blue square shows the field of view from Figure 1, and the orange rectangle shows the region displayed in Figure 6.

The LSB contours are shown in Figure 2. The optical bridge connecting the BCGs and their corresponding plumes extend out to the limiting surface brightness  $\sim 30$  mag arcsec $^{-2}$ . The cirrus clouds extend well beyond the cutout showcased in Figure 1 and pose a risk of overlapping with the ICL, contaminating the signal. To verify that the signal was not contaminated, we computed the observed  $g - r$  color enclosed by the 30 mag arcsec $^{-2}$  contours surrounding BCG1 and the southern cirrus cloud (Figure 1) using the method outlined by J. Román et al. (2020). The color of the cirrus,  $g - r \simeq 0.36 \pm 0.04$ , is consistent with previous studies (J. Román et al. 2020; A. A. Smirnov et al. 2023; J. Zhang et al. 2023) and distinct from the color of the ICL,  $g - r \simeq 0.25 \pm 0.04$ .

### 3.2. Morphology

The LSB features differ significantly from the otherwise elliptical morphology of cluster members. BCG1 features an extended plume to the southeast, enclosing another member (LEDA 64290). The core of BCG2 is enclosed by shells and features two diffuse plumes ( $\sim 30$  mag arcsec $^{-2}$ ) to the northeast and south.

The bridge itself appears to have a rectangular symmetry along a line connecting the cores of BCG1 and BCG2. Several cluster members overlap with the optical bridge, and their extended profiles may contaminate the bridge’s profile. To prevent this from biasing our analysis, we have masked all pixels within  $\sim 53''$  (200 px) of each overlapping cluster member (see right panel Figure 1).

### 3.3. Surface Brightness and Color Profiles

To study the surface brightness and color profiles of the ICL, we used two approaches: fitting isophotes to galaxies and using rectangular bands to measure the bridge’s profile. We fit isophotes to BCG1, BCG2, and LEDA 64218 using the `photutils.isophote` package (L. Bradley et al. 2016) with background sources masked as outlined in Section 2. The

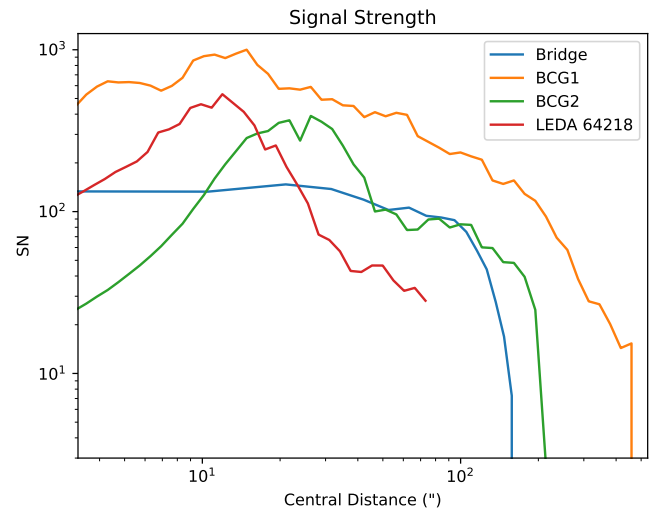


**Figure 3.** The signal-to-noise (SN) of the ICL signal as a function of central distance for different features. The signal for LEDA 64218 is truncated because, beyond  $\sim 100''$ , its outer profile blends into the bridge. Due to the small number of pixels used to fit isophotes near the cores of BCG1, BCG2, and LEDA 64218, the SN profile fluctuates and can have a peak offset from center of the object.

fitting was carried out in two steps: an initial fit allowed the center of each isophote to vary, and a final fit fixed the center at the median center of the initial isophotes. For the bridge, we built a series of rectangular bands that extend parallel to the line connecting BCG1 and BCG2. We assumed rectangular symmetry along this line and measured the bridge’s profile by averaging the flux of the bands at the same distance above and below the line connecting the BCGs. Each profile has been transformed into the rest frame by correcting for extinction (D. J. Schlegel et al. 1998), applying a zero-point correction (Appendix A), a  $K$ -correction (I. V. Chilingarian et al. 2010; I. V. Chilingarian & I. Y. Zolotukhin 2012), and correcting for cosmological surface brightness dimming.



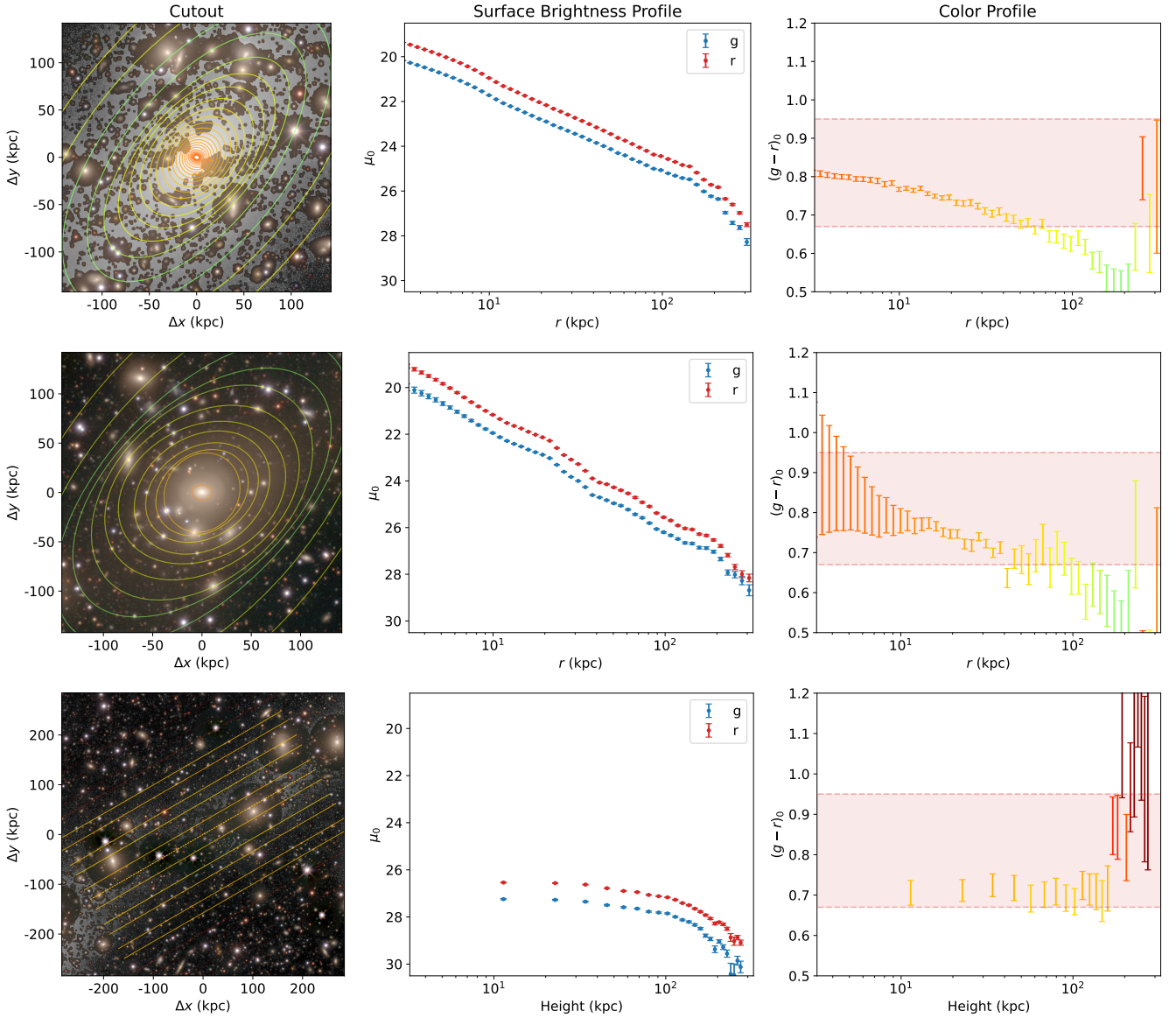


**Figure 4.** The calibrated surface brightness and color profiles for BCG1 (top), BCG2 (middle), and the bridge (bottom). The red shaded region in the color profiles covers the red sequence of A3667 (S. Fu et al. 2024). The isophotes and annuli are drawn over  $grz$  RGB cutouts and colored according to  $(g-r)_0$ . BCG1 is cropped to the core with the mask built in Section 2 applied. We have rendered BCG2 without the mask and central isophotes to showcase the shells surrounding its core. The bridge has the modified LSP mask (detections, bad pixels, stars, and intermediate galaxies) applied and the center contour ( $h=0$ ), is rendered with a dashed line.

To quantify the significance of the ICL signal, we define the signal-to-noise (SN) ratio per isophote (or band) as the ratio between the mean flux ( $f$ ) and error on the mean flux ( $\sigma_f$ ):  $SN = \frac{f}{\sigma_f}$ . The signal drops below our threshold for significance ( $SN \lesssim 3$ ) at a distance of  $\sim 150''$  (160 kpc) for the bridge, at a radius  $\sim 400''$  (430 kpc) for BCG1, and at a radius of  $\sim 200''$  (200 kpc) for BCG2 (Figure 3). These endpoints correspond to an observed surface brightness of  $\sim 30 \text{ mag arcsec}^{-2}$  (Figure 2), consistent with the limiting surface brightness of the observations.

The profiles of BCG1, BCG2, and the bridge are presented in Figure 4, and the profile of LEDA 64218 is presented in Figure 5. The surface brightness profiles surrounding BCG1 and BCG2 transition to the ICL at a radius of  $\sim 100$  kpc, signaled by reaching a surface brightness dimmer than  $\mu \sim 26 \text{ mag arcsec}^{-2}$  and a downturn in the profile. The profile of BCG1 appears consistent with previous studies

(M. Montes & I. Trujillo 2014, 2018), but the profile of BCG2 is disrupted due to the shells surrounding its core at  $r \sim 20\text{--}50$  kpc (Figure 4). The surface brightness profile of LEDA 64218 changes its behavior at  $\sim 30$  kpc from the core and flattens to match the profile of the bridge at  $\sim 70$  kpc.

We compute the  $g-r$  color profile of each object (Figures 4 and 5). BCG1 and BCG2 have well-defined negative color gradients of similar slopes. BCG2, however, flattens at a distance of  $\sim 50\text{--}100$  kpc from the core. LEDA 64218 and the bridge are consistent with flat color profiles.

## 4. Discussion and Conclusion

### 4.1. The Buildup of ICL

The steep negative color gradients surrounding BCG1 and BCG2 are consistent with ICL forming via gradual stripping of satellite galaxies (E. Contini et al. 2018). Unfortunately, with only a single color, the corresponding age and metallicity



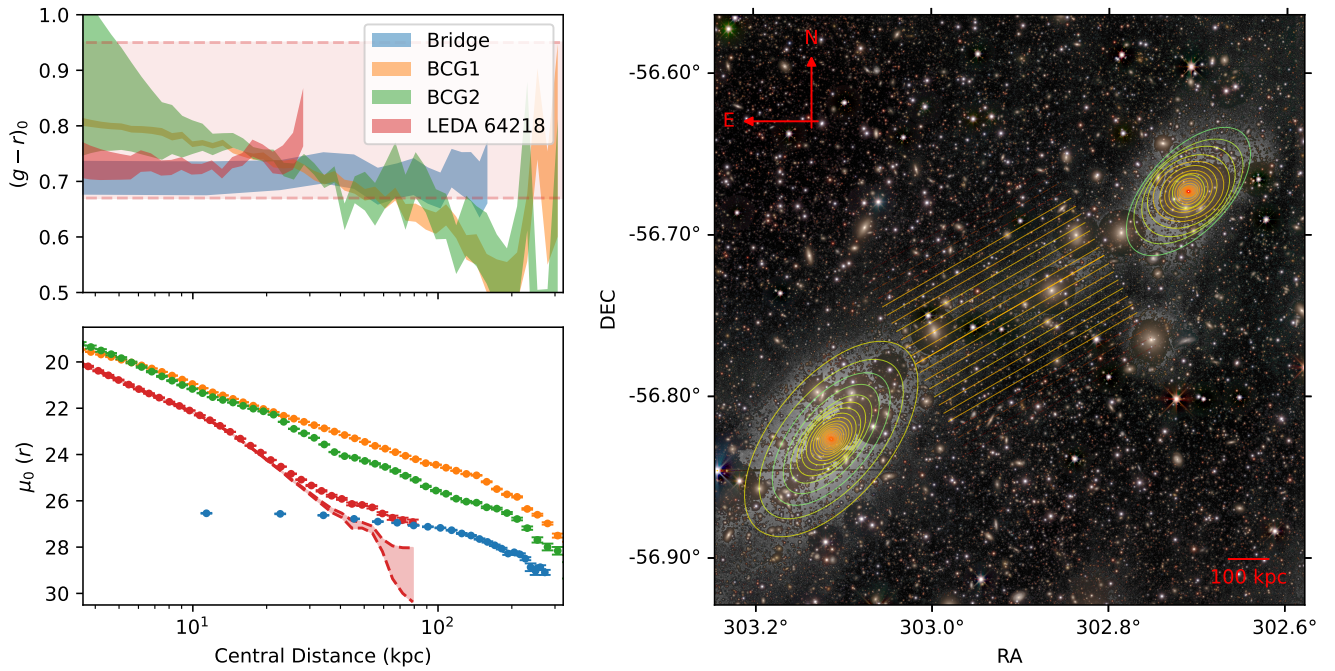


**Figure 5.** Left: the rest-frame  $g - r$  color and  $r$ -band surface brightness profiles; the dashed red curves in the bottom-left panel enclose the profile of LEDA 64218 minus the profile of the bridge. The color profiles have been truncated at smaller central distances for ease of viewing. Right: a cropped cutout of the sky-corrected and star-subtracted image from Figure 1 with statistically significant ( $\text{SN} \gtrsim 3$ ) isophotes and annuli rendered; these are colored per the  $(g - r)_0$  color as in Figure 4.

gradients cannot be studied in detail (e.g., M. Montes et al. 2021). We can partially infer their origin by comparing the color profile to the location of red sequence galaxies (S. Fu et al. 2024), which implies that stars forming the inner 60 kpc (50 kpc) of BCG1 (BCG2) originate from red sequence cluster members.

The color profile in the outer region of BCG2, from  $\sim 50$  to 100 kpc, flattens, implying that the stars in this region have been mixed due to a recent merger that dissolves any potential age or metallicity gradients (E. Contini 2021). The bridge also has a flat color profile, implying that it has also been formed from a recent merger. On an initial inspection, it is unclear if the stars composing the bridge originate from BCG2.

There are two likely scenarios under which the bridge could form: stars may be stripped from one BCG, or galaxies between the BCGs are being stripped due to tidal forces across the cluster. These scenarios can be distinguished using the color of the bridge relative to other cluster members. The color of the bridge is consistent with the mixed region of BCG2 and does not significantly overlap with the color of LEDA 64218; moreover, it is significantly larger than LEDA 64218 and other intermediate galaxies along the bridge, implying that the stars forming the bridge originate from BCG2. This is further supported when studying the profile of LEDA 64218 after the bridge has been subtracted. The profile is not disrupted, implying that stars in its outer regions are not accreting to form the bridge (Figure 5).

#### 4.2. The Formation of A3667

Based on this, we hypothesize that A3667 is in the early stages of its merger, with BCG1 and BCG2 having undergone a nearly radial first pass. During this pass, BCG2 was disrupted by the merger, which led to the formation of shells around its core along with the extended plumes present in both BCGs (L. M. Valenzuela & R.-S. Remus 2024). The merger has

disrupted BCG2, mixing its stars and partially flattening its color profile. The resulting tidal forces have begun stripping stars from BCG2 that may be accreting onto BCG1, resulting in a flat color profile across the bridge.

Radio and X-ray observations of A3667 also support this hypothesis, with the current leading explanation being that A3667 is the product of an offset merger with a small impact parameter (Y. Omiya et al. 2024). The accretion of stars onto BCG1 can be confirmed if the color profile of BCG1 increases to match the color of the bridge. We see an increase in BCG1’s color at a distance of  $\sim 200$  kpc from the core, but the ICL signal rapidly decays in this region, so we do not definitively detect accretion.

#### 4.3. Conclusion

Observations of equivalent depth, taken by LSST, are at least a decade away, leaving the coadds presented here as the deepest optical images of this field. In a future paper, we intend to carry out a full-spectrum analysis of this cluster, which will use optical, X-ray, radio, and submillimeter observations (through the Sunyaev–Zel’dovich effect, R. A. Sunyaev & Y. B. Zeldovich 1970, 1972; R. A. Sunyaev & I. B. Zeldovich 1980) to determine the dynamical history of A3667. These will be compared with the latest simulations and used to study the initial conditions required to produce LSB features such as the bridge.

Upcoming observations of A3667 among other local clusters by LSST are set to transform ICL studies by reaching and potentially exceeding the limiting surface brightnesses reached in this Letter with at least six bands of photometry. This will place tight constraints on the age and metallicity gradients of the ICL, which could directly explain the origin and composition of features like A3667’s bridge. In preparation for this, multiple teams are advancing background and star-subtraction algorithms (The LSST Dark Energy Science Collaboration et al. 2018; L. S. Kelvin et al. 2023;

A. E. Bazkiaei et al. 2024; A. E. Watkins et al. 2024), exploring methods of modeling and subtracting galactic cirrus from LSST-like images (J. Román et al. 2020; A. A. Smirnov et al. 2023; Q. Liu et al. 2025) and considering new methods for analyzing the ICL (Y. Jiménez-Teja et al. 2018; A. Ellien et al. 2021; S. Brough et al. 2024). Altogether, LSST observations will help constrain the stellar population of the ICL while also enabling detailed studies of the dynamical history of local clusters.

### Acknowledgments

We would like to thank the anonymous reviewer for their comments. We would also like to thank the Observational Cosmology and Cluster Weak Lensing Group at Brown University and the Local Volume Complete Cluster Survey for their feedback on an earlier draft. The authors would like to give a special thanks to Jacqueline McCleary, Michael Cooper, Brittany Torres, and Shenming Fu for their thorough comments on the earliest version of this draft.

A.E. acknowledges ongoing support from the NASA Rhode Island Space Grant Consortium.

I.D. and A.E. acknowledge support from the National Science Foundation (No. AST-2108287; Collaborative Research; LoVoCCS). I.D. and A.E. also acknowledge prior support from the U.S. Department of Energy, Office of Science under Award Number DE-SC-0010010.

M.M. acknowledges support from grant RYC2022-036949-I financed by the MICIU/AEI/10.13039/501100011033 and by ESF+, and program Unidad de Excelencia María de Maeztu CEX2020-001058-M.

This project used data obtained with the Dark Energy Camera (DECam), which was constructed by the Dark Energy Survey (DES) collaboration. Funding for the DES Projects has been provided by the DOE and NSF (USA), MISE (Spain), STFC (UK), HEFCE (UK), NCSA (UIUC), KICP (U. Chicago), CCAPP (Ohio State), MIFPA (Texas A&M), CNPQ, FAPERJ, FINEP (Brazil), MINECO (Spain), DFG (Germany) and the Collaborating Institutions in the Dark Energy Survey, which are Argonne Lab, UC Santa Cruz, University of Cambridge, CIEMAT-Madrid, University of Chicago, University College London, DES-Brazil Consortium, University of Edinburgh, ETH Zürich, Fermilab, University of Illinois, ICE (IEEC-CSIC), IFAE Barcelona, Lawrence Berkeley Lab, LMU München and the associated Excellence Cluster Universe, University of Michigan, NSF NOIRLab, University of Nottingham, Ohio State University, OzDES Membership Consortium, University of Pennsylvania, University of Portsmouth, SLAC National Lab, Stanford University, University of Sussex, and Texas A&M University.

Based on observations made at NSF Cerro Tololo Inter-American Observatory, NSF NOIRLab (Appendix C), which is managed by the Association of Universities for Research in Astronomy (AURA) under a cooperative agreement with the U.S. National Science Foundation.

This research draws upon DECam data as distributed by the Astro Data Archive at NSF NOIRLab.

This Letter makes use of LSST Science Pipelines software developed by the Vera C. Rubin Observatory.<sup>5</sup> We thank the Rubin Observatory for making their code available as free software at <https://pipelines.lsst.io>.

This research was conducted using computational resources and services at the Center for Computation and Visualization, Brown University.

*Facility:* Blanco, Astro Data Archive.

*Software:* LSST Science Pipelines (J. Bosch et al. 2018, 2019), *astropy* (Astropy Collaboration et al. 2022), *photutils* (L. Bradley et al. 2016), *numpy* (C. R. Harris et al. 2020), *scipy* (P. Virtanen et al. 2020), *matplotlib* (J. D. Hunter 2007), Source Extractor (E. Bertin & S. Arnouts 1996).

### Appendix A Photometry and Depth

Our full procedure for photometric calibration is discussed in S. Fu et al. (2022), but we briefly review the key details here. Following instrumental-signal removal, each detector was calibrated using reference stars matched with the appropriate filter in SkyMapper DR2 (with the exception of the *u* band, which we matched with SkyMapper’s *v* band; C. A. Onken et al. 2019). After stacking, we derived a per-band linear zero-point correction by transforming the DECam magnitudes of reference stars to SkyMapper with the appropriate color terms. For the *u* band specifically, we used the stellar locus to compute the zero-point correction (F. William High et al. 2009).

The  $5\sigma$  depth is presented in Table 1; based on the point-source depth, we have reached at least LSST year 8 depth.

**Table 1**

The Depth of Our Coadd Based on Point and Extended Sources Selected within  $1^\circ$  from the Peak X-Ray Luminosity of A3667; Estimated with the Median Magnitude of Sources with  $4.5 < \text{SN} < 5.5$

Band	$5\sigma$ PSF	$5\sigma$ CModel	LSST Depth
<i>u</i>	25.2	24.9	Y8
<i>g</i>	26.3	26.1	Y8
<i>r</i>	26.3	26.0	Y8
<i>i</i>	25.8	25.3	Y8
<i>z</i>	25.2	24.8	Y9

**Note.** The magnitude of point and extended sources are measured using PSF and CModel magnitudes, respectively (K. Abazajian et al. 2004).

### Appendix B Sky Correction

Studying ICL typically requires a specialized processing pipeline due to its sensitivity to systematics. This Letter uses a modified version of the *skycorr* algorithm, which is implemented in the LSP (H. Aihara et al. 2019, 2022).<sup>6</sup>

This algorithm depends on the creation of a sky frame for each band, which represents the mean response of DECam to the sky. For this Letter, the sky frames were assembled using a large sample of exposures downloaded from the NOIRLab Astro Data Archive. A sky frame can vary depending on the observing conditions, so we built a selection of exposures whose conditions (e.g., the distribution air masses, moon phases, and moon positions) were consistent with the

<sup>5</sup> <https://rubinobservatory.org/>

<sup>6</sup> [https://github.com/lst/pipe\\_tasks/blob/26.0.0/python/lst/pipe/tasks/skyCorrection.py](https://github.com/lst/pipe_tasks/blob/26.0.0/python/lst/pipe/tasks/skyCorrection.py)



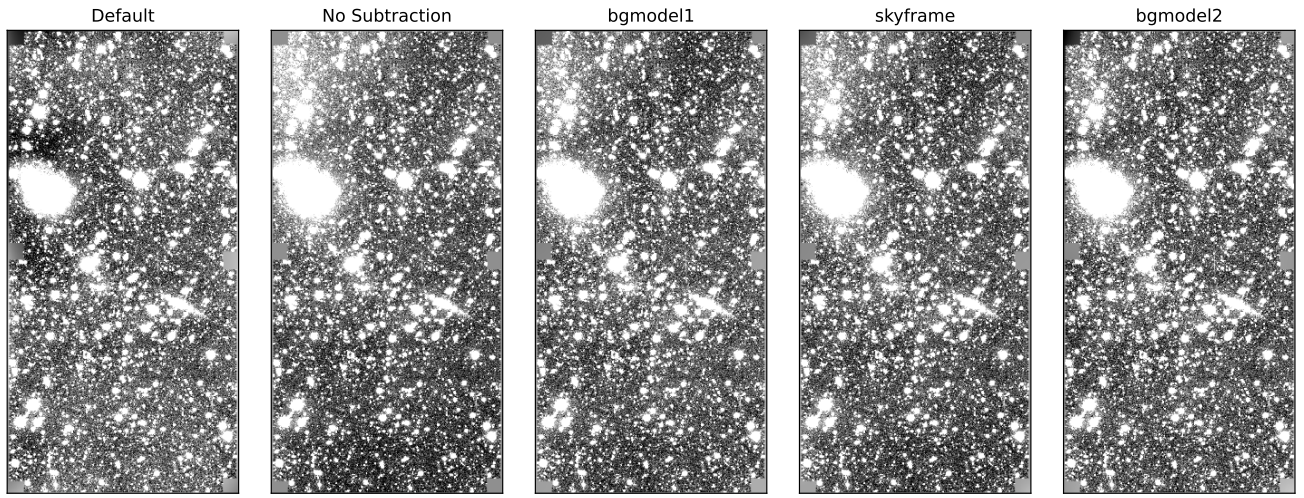


**Figure 6.** Detector 42 from DECam visit 1110874, binned into  $8 \text{ px} \times 8 \text{ px}$  superpixels with an aggressive stretch, shown during different steps of *skycorr*. From left to right: the default *calexp* produced by the LSP with an aggressive background subtraction, the same *calexp* with the background restored, *calexp-bg1*, *calexp-bg1-sky*, and *calexp-bg1-sky-bg2*. The default background model has a pronounced dark ring around a pair of merging galaxies. Without any model, there is a gradient across the detector. This is corrected by *bg1* and the sky frame while preserving the LSB features such as the extended profile of the merging galaxy and the wings of a bright star outside the field of view (top left). *bg2* does not noticeably flatten the background further and removes light from the LSB features.

conditions during the observation of A3667. We removed exposures separated by  $<1^\circ$  and within  $15^\circ$  of the galactic plane. This left  $\sim 200$  exposures per band, which were stacked to create each sky frame using the LSP's calibration-products pipeline (see Section 2).

The steps of *skycorr* are demonstrated in Figure 6; there are four key parts:

1. The background of a calibrated exposure (*calexp*), which is stored separate from the exposure itself in the LSP, is restored.
2. Background pixels are binned into  $4096 \text{ px} \times 4096 \text{ px}$  ( $\sim 1000'' \times 1000''$ ) superpixels. These are smoothly interpolated across the focal plane and subtracted from each detector (*bg1*). This is intended to remove large-scale gradients due to the moon and other sources of scattered light.
3. Background pixels are binned into  $32 \text{ px} \times 32 \text{ px}$  ( $8'' \times 8''$ ) superpixels. The sky frame (*sky*) is fitted to these superpixels across the focal plane, which is then interpolated and subtracted from each detector. This is intended to remove scattered light features that are fixed in the focal plane, such as the "ghost-pupil" (see Figure 4 of H. Aihara et al. 2019 or Figure 4 of G. M. Bernstein et al. 2017 for examples on HSC and DECam, respectively).
4. Background pixels are binned into  $256 \text{ px} \times 256 \text{ px}$  superpixels. These are smoothly interpolated across the focal plane and subtracted from each (*bg2*). This is intended to remove small-scale features that are not modeled by the sky frame.

These steps are iterated and, after each round of subtraction, source detection is ran again, and the detection masks are updated for the next iteration (Figure 7); the mask and background typically converge after two iterations. Fitting and subtraction are done using coordinates in the focal plane where the background is continuous. The results of this algorithm are showcased in Figure 6. The default background model used by

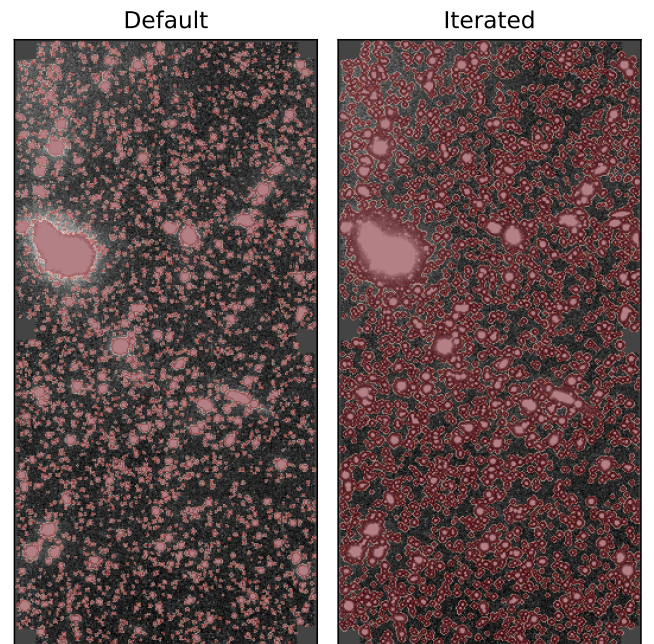


**Figure 7.** Detector 42 from DECam visit 1110874, shown with the default mask produced by the LSP and the final mask created by *skycorr* overlaid in red. The final mask is significantly more aggressive but still fails to mask the most extended features, such as the wings of bright stars and the extended profile of the merging galaxies. This leaves them susceptible to over-subtraction by *bgmodel2*.

the LSP aggressively oversubtracts, producing dark halos around large objects with extended features. The combination of *bg1* and the sky frame successfully flattens the background, without noticeably removing the light of the extended features. However, *bg2* noticeably subtracts extended features larger than its superpixels. Since the bridge extends well beyond the size of the superpixels used for *bg2*, we disabled it for this Letter.



### Appendix C Proposal Information

A table of the proposals and total exposure times used in this Letter is provided in Table 2. Over the past decade, A3667 has been observed with DECam by LoVoCCS and Weighing the Giants (A. von der Linden et al. 2014). Moreover, A3667 lies

in both the Dark Energy Survey (The Dark Energy Survey Collaboration et al. 2016) and DeROSITA Survey (M. Salvato et al. 2022) footprints. Combined with stray pointings from time-domain surveys and smaller projects, A3667 has accrued  $\sim 32$  hr exposure time in total.

**Table 2**

Datasets Queried from the NOIRLab Astro Data Archive That Were Coadded for This Letter along with the Total Exposure Time per Band in Seconds

Proposal ID	PI	<i>u</i>	<i>g</i>	<i>r</i>	<i>i</i>	<i>z</i>
2012B-0001	J. Frieman	...	8280	6480	4680	6390
2013A-0400	J. Bloom	...	...	...	...	1040
2013A-9999	A. Walker	...	...	30	...	...
2014A-0390	J. Bloom	...	...	...	...	480
2014A-0415	A. von der Linden	3355	2355	4010	7850	...
2014A-0624	H. Jerjen	...	720	720	...	...
2014B-0244	A. von der Linden	...	...	3355	560	6980
2015A-0618	C. Lidman	1000	500	500	500	1520
2016A-0397	A. von der Linden	2606	4935	3435	3685	5760
2018A-0242	K. Bechtol	...	...	1890	1260	...
2019A-0308	I. Dell’Antonio	7360	3625	3740	2250	...
2022A-597406	A. Zenteno	...	1800	1800	400	...
2022A-975778	K. Kelkar	...	6000	3900	...	...
2023A-585032	A. Zenteno	810	...	...	...	...
2023B-646244	A. Chiti	...	90	...	...	...
...	Total	15131	28305	29560	21185	22170

## ORCID iDs

Anthony M. Englert  <https://orcid.org/0000-0003-2314-5336>

Ian Dell'Antonio  <https://orcid.org/0000-0003-0751-7312>

Mireia Montes  <https://orcid.org/0000-0001-7847-0393>

## References

- Abazajian, K., Adelman-McCarthy, J. K., Agüeros, M. A., et al. 2004, *AJ*, **128**, 502
- Aihara, H., AlSayyad, Y., Ando, M., et al. 2019, *PASJ*, **71**, 114
- Aihara, H., AlSayyad, Y., Ando, M., et al. 2022, *PASJ*, **74**, 247
- Aihara, H., Arimoto, N., Armstrong, R., et al. 2018, *PASJ*, **70**, S4
- Allen, S. W., Evrard, A. E., & Mantz, A. B. 2011, *ARA&A*, **49**, 409
- Alonso Asensio, I., Dalla Vecchia, C., Bahé, Y. M., Barnes, D. J., & Kay, S. T. 2020, *MNRAS*, **494**, 1859
- Astropy Collaboration, Price-Whelan, A. M., Lim, P. L., et al. 2022, *ApJ*, **935**, 167
- Bazkiaei, A. E., Kelvin, L. S., Brough, S., et al. 2024, arXiv:2404.04802
- Bernstein, G. M., Abbott, T. M. C., Desai, S., et al. 2017, *PASP*, **129**, 114502
- Bertin, E., & Arnouts, S. 1996, *A&AS*, **117**, 393
- Bianco, F. B., Ivezić, Z., Jones, R. L., et al. 2022, *ApJS*, **258**, 1
- Borlaff, A., Trujillo, I., Román, J., et al. 2019, *A&A*, **621**, A133
- Bosch, J., AlSayyad, Y., Armstrong, R., et al. 2019, in ASP Conf. Ser. 523, *Astronomical Data Analysis Software and Systems XXVII*, ed. P. J. Teuben et al. (San Francisco, CA: ASP), 521
- Bosch, J., Armstrong, R., Bickerton, S., et al. 2018, *PASJ*, **70**, S5
- Bradley, L., Sipocz, B., Robitaille, T., et al. 2016, Photutils: Photometry tools, *Astrophysics Source Code Library*, ascl:1609.011
- Brough, S., Ahad, S. L., Bahé, Y. M., et al. 2024, *MNRAS*, **528**, 771
- Broughton, A., Utsumi, Y., Plazas Malagón, A. A., et al. 2024, *PASP*, **136**, 045003
- Burke, C., Hilton, M., & Collins, C. 2015, *MNRAS*, **449**, 2353
- Carretti, E., Brown, S., Staveley-Smith, L., et al. 2013, *MNRAS*, **430**, 1414
- Cha, S., Cho, B. Y., Joo, H., et al. 2025, arXiv:2503.21870
- Chilingarian, I. V., Melchior, A.-L., & Zolotukhin, I. Y. 2010, *MNRAS*, **405**, 1409
- Chilingarian, I. V., & Zolotukhin, I. Y. 2012, *MNRAS*, **419**, 1727
- Clowe, D., Bradač, M., Gonzalez, A. H., et al. 2006, *ApJ*, **648**, L109
- Contini, E. 2021, *Galax*, **9**, 60
- Contini, E., Yi, S. K., & Kang, X. 2018, *MNRAS*, **479**, 932
- Coulton, W. R., Armstrong, R., Smith, K. M., Lupton, R. H., & Spergel, D. N. 2018, *AJ*, **155**, 258
- de Gasperin, F., Rudnick, L., Finoguenov, A., et al. 2022, *A&A*, **659**, A146
- DeMaio, T., Gonzalez, A. H., Zabludoff, A., Zaritsky, D., & Bradač, M. 2015, *MNRAS*, **448**, 1162
- DeMaio, T., Gonzalez, A. H., Zabludoff, A., et al. 2018, *MNRAS*, **474**, 3009
- Diego, J. M., Pascale, M., Frye, B., et al. 2023, *A&A*, **679**, A159
- Ellien, A., Montes, M., Ahad, S. L., et al. 2025, *A&A*, **698**, A134
- Ellien, A., Slezak, E., Martinet, N., et al. 2021, *A&A*, **649**, A38
- Englert, A., Dell'Antonio, I., Fu, S., et al. 2024, in Rubin Community Workshop 2024, LoVoCCS: Applications of LSST Science Pipeline Processed DECam Observations, <https://project.lsst.org/meetings/rubin-2024/lovoccs-applications-lsst-science-pipeline-processed-decam-observations>
- Englert, A., Dell'Antonio, I., Fu, S., et al. 2025, AAS Meeting, **245**, 412.07
- Feldmeier, J. J., Mihos, J. C., Morrison, H. L., Rodney, S. A., & Harding, P. 2002, *ApJ*, **575**, 779
- Finner, K., Jee, M. J., Cho, H., et al. 2025, *ApJS*, **277**, 28
- Flaugher, B., Diehl, H. T., Honscheid, K., et al. 2015, *AJ*, **150**, 150
- Fu, S., Dell'Antonio, I., Chary, R.-R., et al. 2022, *ApJ*, **933**, 84
- Fu, S., Dell'Antonio, I., Escalante, Z., et al. 2024, *ApJ*, **974**, 69
- Gaia Collaboration, Vallenari, A., Brown, A. G. A., et al. 2023, *A&A*, **674**, A1
- Gonzalez, A. H., George, T., Connor, T., et al. 2021, *MNRAS*, **507**, 963
- Gonzalez, A. H., Zabludoff, A. I., & Zaritsky, D. 2005, *ApJ*, **618**, 195
- Harris, C. R., Millman, K. J., van der Walt, S. J., et al. 2020, *Natur*, **585**, 357
- Harvey, D., Massey, R., Kitching, T., Taylor, A., & Tittley, E. 2015, *Sci*, **347**, 1462
- Hunter, J. D. 2007, *CSE*, **9**, 90
- Infante-Sainz, R., Trujillo, I., & Román, J. 2020, *MNRAS*, **491**, 5317
- Iodice, E., Spavone, M., Cantiello, M., et al. 2017, *ApJ*, **851**, 75
- Jiménez-Teja, Y., Dupke, R., Benítez, N., et al. 2018, *ApJ*, **857**, 79
- Jiménez-Teja, Y., Román, J., HyeonHan, K., et al. 2025, *A&A*, **694**, A216
- Kelvin, L. S., Hasan, I., & Tyson, J. A. 2023, *MNRAS*, **520**, 2484
- Kluge, M., Neureiter, B., Riffeser, A., et al. 2020, *ApJS*, **247**, 43
- Kravtsov, A. V., & Borgani, S. 2012, *ARA&A*, **50**, 353
- Lee, W., Pillepich, A., ZuHone, J., et al. 2024, *A&A*, **686**, A55
- Li, J., Huang, S., Leauthaud, A., et al. 2022, *MNRAS*, **515**, 5335
- Liu, Q., Abraham, R., Martin, P. G., et al. 2025, *ApJ*, **979**, 175
- Lovisari, L., Kapferer, W., Schindler, S., & Ferrari, C. 2009, *A&A*, **508**, 191
- Luo, Y., Leauthaud, A., Greene, J., et al. 2024, *MNRAS*, **530**, 4988
- Martín, N. S., Sarrouh, G. T. E., Willott, C. J., et al. 2024, *ApJ*, **975**, 76
- Mihos, J. C., Harding, P., Feldmeier, J., & Morrison, H. 2005, *ApJL*, **631**, L41
- Mihos, J. C., Harding, P., Feldmeier, J. J., et al. 2016, *ApJ*, **834**, 16
- Moffat, A. F. J. 1969, *A&A*, **3**, 455
- Montes, M. 2022, *NatAs*, **6**, 308
- Montes, M., Brough, S., Owers, M. S., & Santucci, G. 2021, *ApJ*, **910**, 45
- Montes, M., & Trujillo, I. 2014, *ApJ*, **794**, 137
- Montes, M., & Trujillo, I. 2018, *MNRAS*, **474**, 917
- Montes, M., & Trujillo, I. 2019, *MNRAS*, **482**, 2838
- Montes, M., & Trujillo, I. 2022, *ApJL*, **940**, L51
- Morishita, T., Abramson, L. E., Treu, T., et al. 2017, *ApJ*, **846**, 139
- Oke, J. B., & Gunn, J. E. 1983, *ApJ*, **266**, 713
- Omiya, Y., Nakazawa, K., Tamura, T., et al. 2024, *A&A*, **689**, A173
- Onken, C. A., Wolf, C., Bessell, M. S., et al. 2019, *PASA*, **36**, e033
- Owers, M. S., Couch, W. J., & Nulsen, P. E. J. 2009, *ApJ*, **693**, 901
- Piffaretti, R., Arnaud, M., Pratt, G. W., Pointecouteau, E., & Melin, J. B. 2011, *A&A*, **534**, A109
- Román, J., Trujillo, I., & Montes, M. 2020, *A&A*, **644**, A42
- Salvato, M., Wolf, J., Dwelly, T., et al. 2022, *A&A*, **661**, A3
- Sampaio-Santos, H., Zhang, Y., Ogando, R. L. C., et al. 2021, *MNRAS*, **501**, 1300
- Sarazin, C. L. 1986, *RvMP*, **58**, 1
- Schlegel, D. J., Finkbeiner, D. P., & Davis, M. 1998, *ApJ*, **500**, 525
- Smirnov, A. A., Savchenko, S. S., Poliakov, D. M., et al. 2023, *MNRAS*, **519**, 4735
- Storm, E., Vink, J., Zandanel, F., & Akamatsu, H. 2018, *MNRAS*, **479**, 553
- Sunyaev, R. A., & Zeldovich, I. B. 1980, *ARA&A*, **18**, 537
- Sunyaev, R. A., & Zeldovich, Y. B. 1970, *ApSS*, **7**, 3
- Sunyaev, R. A., & Zeldovich, Y. B. 1972, *CoASP*, **4**, 173
- The Dark Energy Survey Collaboration, Abbott, T., Abdalla, F. B., et al. 2016, *MNRAS*, **460**, 1270
- The LSST Dark Energy Science Collaboration, Mandelbaum, R., Eifler, T., et al. 2018, arXiv:1809.01669
- Trujillo, I., & Fliri, J. 2016, *ApJ*, **823**, 123
- Valenzuela, L. M., & Remus, R.-S. 2024, *A&A*, **686**, A182
- van Weeren, R. J., de Gasperin, F., Akamatsu, H., et al. 2019, *SSRv*, **215**, 16
- Virtanen, P., Gommers, R., Oliphant, T. E., et al. 2020, *NatMe*, **17**, 261
- von der Linden, A., Allen, M. T., Applegate, D. E., et al. 2014, *MNRAS*, **439**, 2
- Watkins, A. E., Kaviraj, S., Collins, C. C., et al. 2024, *MNRAS*, **528**, 4289
- William High, F., Stubbs, C. W., Rest, A., Stalder, B., & Challis, P. 2009, *AJ*, **138**, 110
- Yoo, J., Ko, J., Sabiu, C. G., et al. 2022, *ApJS*, **261**, 28
- Yoo, J., Park, C., Sabiu, C. G., et al. 2024, *ApJ*, **965**, 145
- Zhang, J., Martin, P. G., Cloutier, R., et al. 2023, *ApJ*, **948**, 4
- Zhang, Y., Yanny, B., Palmese, A., et al. 2019, *ApJ*, **874**, 165